

1 **Deposition of light-absorbing particles in glacier snow of the Sunderdhunga Valley, the**
2 **southern forefront of Central Himalaya**

3

4 Jonas Svensson^{1,2}, Johan Ström³, Henri Honkanen⁴, Eija Asmi¹, Nathaniel B. Dkhar⁵, Shresth
5 Tayal^{5,6}, Ved P. Sharma^{5,6}, Rakesh Hooda¹, Matti Leppäranta⁴, Hans-Werner Jacobi², Heikki
6 Lihavainen^{7,1}, Antti Hyvärinen¹

7 1 Atmospheric Composition Research, Finnish Meteorological Institute, Helsinki, Finland

8 2 Université Grenoble Alpes, CNRS, IRD, INP-G, IGE, Grenoble, France

9 3 Department of Environmental Science, Stockholm University, Stockholm, Sweden

10 4 Institute for Atmospheric and Earth System Research, Faculty of Science, University of Helsinki,
11 Helsinki, Finland

12 5 The Energy and Resource Institute, (TERI), New Delhi, India

13 6 TERI School of Advanced Studies (TERI SAS), New Delhi, India

14 7 Svalbard Integrated Arctic Earth Observing System, Longyearbyen, Norway

15

16 Correspondence to: jonas.svensson@fmi.fi

17

18 Abstract

19 Anthropogenic activities on the Indo-Gangetic Plain emit vast amounts of light-absorbing particles
20 (LAP) into the atmosphere, modifying the atmospheric radiation state. With transport to the nearby
21 Himalayan mountains and deposition to its surfaces the particles contribute to glacier and snowmelt via
22 darkening of the highly reflective snow. The Central Himalayas have been identified as a region where
23 LAP are especially pronounced in glacier snow, but still remain a region where measurements of LAP
24 in the snow are scarce. Here we study the deposition of LAP in five snow pits sampled in 2016 (and
25 one from 2015) within one km from each other from two glaciers in the Sunderdhunga valley, state of
26 Uttarakhand, India, Central Himalaya. The snow pits display a distinct enriched LAP layer interleaved
27 by younger snow above, and older snow below. The LAP exhibit a distinct vertical distribution in these
28 different snow layers. For the analyzed elemental carbon (EC), the younger snow layers in the different
29 pits show similarities, which can be characterized by a deposition constant of about $50 \mu\text{g m}^{-2}$ per mm^{-1}
30 $^{\pm}$ snow water equivalent (SWE) while the old snow layers also indicate similar values, described by a
31 deposition constant of roughly $150 \mu\text{g m}^{-2}$ per mm^{-1} SWE. The enriched LAP layer, contrarily, display
32 no similar trends between the pits. Instead, it is characterized by very high amounts of LAP, and differ
33 in orders of magnitude for concentration between the pits. The enriched LAP layer is likely a result of
34 strong melting that took place during the summers of 2015 and 2016, as well as possible lateral transport
35 of LAP. The mineral dust fractional absorption is slightly below 50 % for the young and old snow layer,

36 whereas it is the dominating light absorbing constituent in the enriched LAP layer, thus, highlighting
37 the importance of dust in the region. Our results indicate the problems with complex topography in the
38 Himalaya, but nonetheless, can be useful in large-scale assessments of LAP in Himalayan snow.

39 1 Introduction

40 Aerosol particles in the Indo-Gangetic Plain (IGP) are produced in great mass and number. Being
41 especially prominent in the pre-monsoon season, a large fraction of the airborne aerosols are
42 carbonaceous particles, consisting of organic carbon (OC) and black carbon (BC). Originating from the
43 combustion of fossil fuels and biomass, the particles form the atmospheric brown cloud—known to
44 modify the atmospheric radiation state (Lau et al., 2006; Menon et al., 2010; Ramanathan and
45 Carmichael, 2008). Through air mass transport the aerosol can be conveyed and lifted from the IGP to
46 its northern barrier, the mountains of Himalaya (e.g. Hooda et al., 2018; Kopacz et al., 2011;
47 Raatikainen et al., 2014; Zhang et al., 2015). Covered with vast amounts of snow and ice, the Himalayan
48 cryosphere is affected by the deposition of carbonaceous aerosol onto its surface (e.g. He et al., 2018;
49 Jacobi et al., 2015; Ménégoz et al., 2014; Xu et al., 2009). This is due to the particulates and especially
50 BC effectiveness in reducing the snow albedo (Warren and Wiscombe, 1980), which ultimately leads
51 to accelerated snow melt (Flanner et al., 2007; Jacobi et al., 2015; Jacobson, 2004; Ming et al., 2012).

52

53 In addition to BC and OC, other particles such as mineral dust (MD) and snow microbes (collectively
54 known as light-absorbing particles (LAP)) are also of importance in reducing snow albedo (e.g. Skiles
55 et al. 2018). In Himalayan snow and ice, the LAP content has been shown to vary significantly, both
56 spatially and temporally (e.g. see review by Gertler et al., 2016). Further, an extensive compilation of
57 BC measurements in snow over the Tibetan Plateau is presented in the supplement of He et al. (2018),
58 with concentrations ranging from 1 to 3600 ppb_w in the region termed as Himalaya. In addition to long
59 range transported LAP, local sources within the Tibetan plateau have also been documented to be
60 significant in some regions (e.g. Li et al., 2016), creating several different sources of LAP in the snow.
61 Varying meteorology and terrain induced exchange processes (advection and turbulence) in the
62 mountains further complicates the interplay between the atmospheric deposition of LAP and the snow
63 surfaces.

64

65 Recent modeling studies have reported analogous results, indicating certain sub-regions of the
66 Himalaya to be especially vulnerable to LAP deposition. Santra et al. (2019) simulated the BC impact
67 on snow albedo and glacier runoff in the Hindu Kush-Himalaya region. The authors identified a hot-
68 spot zone for BC in the vicinity of Manora peak, located in the Indian state of Uttarakhand, central
69 Himalaya (also sometimes called western Himalaya depending on classification). The BC induced a
70 greater albedo reduction on glacier snow in the vicinity of this hot spot area compared to other areas in
71 the Hindu Kush-Himalayan area. Similarly, another modeling study simulated the impact of LAP on
72 High Mountain Asia snow albedo and its associated forcing and identified the same general area as a
73 region where snow is especially affected by LAP-caused snow darkening (Sarangi et al., 2019). Both

74 of these studies (as well as the work of He et al., 2018) emphasized the need for more *in situ*
75 measurements of LAP in the snow of this region of the Himalaya.

76

77 Previously, we reported in Svensson et al. (2018) the measured LAP concentrations and properties in
78 the snow from two glaciers in the Sunderdhunga valley, located in Uttarakhand, India, central Himalaya.
79 While we mainly focused on the surface snow layer and characterizing the LAP, results from one 1.2
80 m deep snow pit were also presented. Based on the LAP concentration profile and pit stratigraphy, the
81 pit was estimated to represent 5 seasons. Newly sampled snow pits have since then been analyzed from
82 the same two glaciers, along with available automatic weather station (AWS) data from the same valley.
83 Here we revisit the previous interpretation of the published pit (in Svensson et al., 2018), and report the
84 results of our newly sampled snow pits. By comparing the BC profiles among 6 pits we aim at
85 quantifying the deposition of elemental carbon (EC; used here as a proxy for BC) in this area of the
86 Himalaya. In addition, we explore the relative contribution of MD to LAP in the different pits.

87

88 2 Methodology

89 2.1 Glaciers snow sampling and filtration

90 Snow was collected on Bhanolti and Durga Kot glaciers during a field campaign in the Sunderdhunga
91 valley (located in the Bageshwar district) in October of 2016. The two glaciers are positioned adjacent
92 to each other in a general northeast-southwest orientation (cf. Fig. 1) on the southern fringe of the
93 Himalayan mountain range and are further described in Svensson et al. (2018). Local emissions of
94 carbonaceous aerosol in the Sunderdhunga valley are very limited. The valley is not accessible by car
95 and the glaciers are at a three to four-day hike from the nearest road. On route to the glaciers the last
96 settlement is Jatoli, located in a river valley at an elevation of 2400 m. a.s.l. about 10 km southeast in a
97 perpendicular orientation to the glacier valley. Biomass burning is a common practice for cooking and
98 heating in Jatoli, thus some emissions from the village may enter the glacier valley. It is expected,
99 however, that the majority of carbonaceous particles in the glacier valley originates from regional and
100 long-distance transport. The relatively low elevation span as well as the glaciers' position on the
101 southern slopes of the Himalayan mountains nonetheless, make them more prone to LAP deposition
102 compared to other glaciers in the Himalaya and Tibetan plateau. Previous studies have reported elevated
103 LAP content in lower elevation snow for Himalayan glaciers (e.g. Ming et al., 2013), and higher
104 concentrations of LAPs in glaciers on the southern edge of the Himalaya (e.g. Xu et al., 2009).

105

106 On Durga Kot glacier two snow pits (hereafter Pit A and B; Fig. 1) were dug in the vicinity of each
107 other (~20 m) in an reachable area of the percolation zone of the glacier. Bhanolti glacier was more
108 easily accessible, and the three excavated snow pits (hereafter Pit C, D, E; Fig. 1) were spread out over
109 a greater distance (~500 m) on the glacier (see table 1 and Fig. 1 for additional information). The depth

110 of the pits depended on the level at which a hard layer was found, and digging could not be further
111 conducted with the reinforced shovels with a sharpened edge. The deepest snow pit that was analyzed
112 previously in Svensson et al. (2018), referred to as pit 5 in that study, is from Bhanolti glacier in
113 September of 2015, and we denote as Pit F in the subsequent sections of this manuscript. As for the
114 other pits from 2016, the depth of Pit F was governed by the depth at which the hard layer was
115 encountered.

116
117 Three distinctly different colored snow layers could be observed repeating in all but one of the year
118 2016 pits: a relatively thin (on the order of centimeters) very dark layer was wedged in-between white
119 snow above and more grey appearing snow below (See for e.g. pits B and D in Fig. S1a-b). Due to this
120 stratigraphy, we hereafter simply refer to the whitest snow as young snow, the darkest layer as the
121 enriched LAP layer, and the grey snow as old snow. Representative samples ranging from 3 to 10 cm
122 thick layers were taken throughout each pit for analysis of LAP. Snow density measurements were
123 conducted with a snow density kit in the upper part of the pits (in 5 cm increments) by weighing the
124 known volume of the sampler filled with snow. The observed densities ranged between 0.29 and 0.46
125 g cm^{-3} (see table 1 for details). Density measurements were not possible below the enriched LAP layer
126 due to the hard snow. For these layers the density was assumed 0.5 g cm^{-3} (to represent aged snow) in
127 our further analyzes. Snow density measurements were not conducted for Pit F, and we assigned a
128 density of 0.35 g cm^{-3} for the top layer (0-3 cm; similar to observations made in 2016), followed by 0.4
129 g cm^{-3} between 3-10 cm depth, and 0.5 g cm^{-3} for all layers below 10 cm. Since the snow samples could
130 not be transported in a solid phase back to the laboratory, they were melted and filtered at the nearby
131 base camp using the same principles as in Svensson et al. (2018). Filters were transported back to the
132 analysis laboratory in petri slides.

133

134 2.2 Meteorological observations

135 In September 2015 an AWS was installed next to the glacier ablation zone of Durga Kot (Fig. 1) about
136 1.5 km northwards at an elevation below the snow sampling sites. The AWS is equipped with
137 instruments for air temperature, relative humidity (HC2S3-L Temperature and relative humidity probe
138 manufactured by Rotronic, with 41303-5A Radiation shield), shortwave (SW) and longwave (LW)
139 radiation (upward and downward) (CNR4 Four-component net radiometer manufactured by Kipp &
140 Zonen), wind speed and direction (05103-L Wind monitor manufactured by R. M. Young), and snow
141 depth (Campbell Scientific SR50A-L Ultrasonic Distance Sensor). In this paper we use the snow depth
142 data between September 2015 and September 2017 to estimate the local precipitation. The original snow
143 depth data, logged once every 10 minutes was filtered to daily resolution by applying a moving median
144 window of 24 hours and for the noon value of each day in further analyzes. This filtering removed much
145 of the signal noise. However, before this filtering was applied the data was reduced using several logical

146 conditions such as: the incoming SW radiation is greater than outgoing SW radiation (to remove errors
147 due to sensors covered by snow), and the surface albedo is greater than 0.2 (to ensure snow cover as the
148 ground albedo was measured at 0.17). Finally, the consistency between the daily albedo and snow depth
149 was inspected using data presented in Figure S42a. Each day the snow depth increased was interpreted
150 as precipitation, and to arrive at an estimate of the snow water equivalent (SWE), the fresh snow density
151 is assumed to be 100 kg m^{-3} (Helfricht, et al., 2018). The solid precipitation derived based on the
152 cumulative SWE is presented in Figure S2b.

153

154 2.3 Filter analysis

155 The analysis of filters followed the procedure in Svensson et al. (2018), with transmission
156 measurements coupled with thermal-optical analysis. According to the measurement nomenclature
157 (Petzold et al., 2013), the carbonaceous constituents measured are EC and OC. The measurement
158 method briefly follows the procedure of placing a filter punch in a custom-built particle soot absorption
159 photometer (PSAP) to measure the transmittance (at $\lambda = 526 \text{ nm}$; Krecl et al., 2007)—providing an
160 optical depth for all of the particles captured by the filter. The filter punch is then placed in an OCEC
161 analyzer (Sunset instrument, using the EUSAAR_2 protocol) to determine the OC and EC mass,
162 followed by another measurement with the PSAP. The OCEC analysis removes the carbonaceous
163 species and, thus, by comparing the PSAP results obtained before and after the analysis, the relative
164 contribution of the light absorption by EC particles in the total particles optical depth is obtained. The
165 remaining optical depth we attribute as non-EC material. This fraction of the total optical thickness we
166 report as the percentage of the mineral dust absorption on the filter samples (expressed as f_D). For further
167 details concerning the measurements see Svensson et al (2018).

168

169 Some of the filter samples (N=17, out of 91) were saturated with too much light absorbing material
170 prohibiting reliable EC measurements despite reducing the sample to a melted equivalent of only 30
171 mL. To mitigate this problem, we calculated the EC indirectly from the analyzed total carbon (TC) for
172 the saturated samples. From OCEC analysis TC is the most robust measured constituent, since it
173 includes both OC and EC and is not affected by their split point, which may be incorrectly placed for
174 very dark filters (Chow et al., 2001). A slope of 0.099 for the EC:TC ratio for filter samples considered
175 non-saturated was used to reconstruct the EC content for the filter samples containing high amounts of
176 absorbing particles (see details in supplement and Fig. S33a-b). The slope compares well with the slopes
177 reported for air samples collected at two sites in the Himalayas about 550 km south-east from
178 Sunderdhunga in the Kathmandu valley 32 km (altitude of 2150 m a.s.l.) east of Kathmandu, and
179 Langtang 60 km north of Kathmandu (altitude of 3920 m a.s.l.) (Caricco et al., 2003). There, the authors
180 found that the EC/TC ratio was 0.17 for both sites during the summer monsoon season, but between
181 0.10 and 0.13 during what they described as the ramp-up period and the peak concentration season. The

182 snow samples do not have an upper limit for particles sizes, whereas the air samples were collected as
183 PM2.5 (particulate matter collected below an aerodynamic diameter of 2.5 μm). The slopes are rather
184 similar to our value, and the authors found as well a very strong correlation of 0.89 (r^2) between monthly
185 average EC and OC.

186

187 3 Results and discussion

188 3.1 EC deposition in young and old snow samples

189 When the EC content is analyzed from filtered snow samples, a common practice is to convert the
190 results into mass concentrations [EC], given per volume or mass of melt water (e.g. $\mu\text{g L}^{-1}$ or ng g^{-1}).

191 A spread in results is often largely due to local processes and specific sampling layer thicknesses. The
192 mass deposition per unit area \widetilde{EC} , on the other hand, can be expected to be less variable with increasing
193 number of layers used to calculate this value. The deposition in each layer is calculated according to:

194

$$195 \quad \widetilde{EC}_i = [EC]_i \frac{\rho_s}{\rho_w} d_i \quad (1)$$

196

197 where ρ_s and ρ_w are snow and liquid water densities, respectively. The index i , is the number of the
198 sampled layer from top to bottom, and $\rho_s/\rho_w d$ is the SWE thickness, d_{SWE} . The \widetilde{EC}_i and d_{SWEi} are
199 transformed to cumulative plots by integrating over the layers from the surface to the bottom. These
200 profiles are presented in Fig. 2a-f (with each sampling layer represented by a square).

201

202 The visible snow pit stratigraphy described above in section 2.1 can be observed in the pit profiles. At
203 the top, the accumulated EC (EC_{acc}) as a function of the accumulated d_{SWE} (SWE_{acc}) portray the
204 young snow layers, whereas in the bottom of the pits the data points represent the old snow layers (Fig.
205 2a-f). This pattern (with both young and old snow layers) is visible in pits A, B, C, and D (Fig. 2a-d).
206 These pits also have the enriched LAP layer interleaved between the young and old snow layers,
207 indicated by the sharp increase (or steep slope) between the young and old snow layers. In the two pits
208 where this general outline is not visible (pit E Fig. 2e and pit F Fig. 2f), it can be explained by the fact
209 that pit E extended only to the enriched LAP layer (therefore no old snow samples) while pit F had
210 essentially no young snow samples at the time of sampling (therefore pit F starts with the enriched LAP
211 layer).

212

213 With the data points for young and old snow appearing rather similar in slope between the pits, the
214 homogeneity is emphasized further by comparing the observations with common effective constants
215 for young and old snow (EC_y^* and EC_o^*), respectively. Suitable constants were determined to be close to
216 $50 \mu\text{g m}^{-2}$ per mm SWE for young snow and $150 \mu\text{g m}^{-2}$ per mm SWE for old snow (see supplement

217 section 4). The resulting deposition using EC_y^* and EC_o^* are superimposed over the observations in
 218 Figure 2a-e as dashed lines for young snow and dotted lines for old snow. These lines then represent
 219 the constant deposition of EC as function of accumulated melt water in a column according to:

220

$$221 \quad EC_{acc} = constant * SWE_{acc} + offset \quad (2)$$

222

223 where EC_{acc} is the accumulated EC mass per m^2 and SWE_{acc} is the accumulated melt water in $L m^{-2}$
 224 (or mm), and the ‘constant’ is the deposition constant. The offsets for young snow are a result of
 225 enhanced observed EC concentration in the top layer, which can numerically be compensated for by
 226 “artificially” adding a small value to (ΔSWE_{acc}) to each pit (except pit A), which in essence dilute the
 227 top layer, but have marginal effect on the overall picture. This meant simply rewriting the linear relation
 228 above into:

229

$$230 \quad EC_{acc} = constant * (SWE_{acc} + \Delta SWE_{acc}) \quad (3)$$

231

232 The ΔSWE_{acc} amounts were chosen by trial and error to be in multiples of 10 mm for simplicity. The
 233 resulting values were 10, 650, 20, and 20 mm for pits B through E in order to explain the apparent
 234 offset. A physical interpretation of these numbers may be the loss of water from the surface layer due
 235 to evaporation or sublimation, which enhance $[EC]$ in the top layer. For the old snow layers, snow and
 236 EC were numerically removed in the data by subtracting accumulated EC and SWE (including the
 237 enriched LAP layer, when present) down to the old snow layer. This was done such that the first data
 238 point satisfies EC_o^* . Hence, for old snow $[EC]_1 d_{SWE_1} / EC_o^* = SWE_{acc_1}$ where the index (1) represents the
 239 top layer of old snow.

240

241 By applying the offset values and numerically removing the upper snow layers, we compare the data in
 242 Fig. 2a-f in two separate figures (Fig. 3a-b), one where young snow are grouped together and one for
 243 old snow. In Fig 3a, the observed EC_{acc} is plotted against the EC_{acc} value if EC_y^* is used. In Fig. 3b
 244 the observed EC_{acc} is plotted against the EC_{acc} value if EC_o^* is used. Note that for old snow the first
 245 data point in the different pits will, by definition, be on the 1:1 line. Nevertheless, the consistency
 246 between the pits is striking and the fact that much of the variation in EC_{acc} as function of SWE_{acc} (or
 247 depth in the pit) can be explained by EC_y^* and EC_o^* alone is a very interesting finding.

248

249 3.2 Enriched LAP layer

250 On the contrary to the observed similarities in the different pits between young and old snow, the
 251 enriched LAP layer samples do not display similar trends. Instead of being characterized by a common
 252 constant, the EC_{acc} value as function of SWE_{acc} in the enriched LAP layer differs by orders of

253 magnitude between the different pit profiles. To explore the enriched LAP layers further, we make use
254 of the constant for young snow, EC_y^* . Assuming that this is a characteristic value for precipitation during
255 the winter season, we can estimate the required amount of precipitation (SWE_{acc}) that is needed to
256 explain the observed EC_{acc} deposition. These derived precipitation amounts for each pit are presented
257 in Figure 4 as a function of the relative depth from the surface to the bottom of the pit. Using this
258 approach, pit F corresponds to a total equivalent of about 2200 mm in precipitation, whereas pits B, E,
259 and D represent 32800, 4200, and 4900 mm, respectively. Pits A and C deviate starkly from the others,
260 with 36000 and 54000 mm precipitation. Comparing these derived values to other precipitation
261 estimates allows us to provide a temporal perspective required to explain the observed EC in the pits.
262 Other studies have shown that the annual precipitation is very altitude-level dependent in the Himalayas,
263 and based on the altitude of the glaciers alone one would expect less than about 1000 mm in annual
264 precipitation (Anders et al., 2006; Bookhagen and Burbank, 2010). Based on the changes in snow depth,
265 the local precipitation was estimated using the AWS as described in section 2.2. This analysis gave a
266 snow accumulation of about 600 mm SWE in the winter season 2015-2016 and 700 mm in the 2016-
267 2017 winter season at the location of the AWS. Over the season, a fraction of the snow evaporates or
268 sublimates, possibly accounting for a magnitude of mm per day during favorable conditions (Stigter et
269 al., 2018). Further, Mimeau et al. (2019) estimated the sublimation between 12 and 15 % of the total
270 annual precipitation in the Khumbu valley, Nepal. This amount might be missed by this method using
271 daily data. Nonetheless, our two precipitation estimates are below the observed annual precipitation of
272 976 mm in 2012/2013 at 3950 m altitude, about 250 km to the north-west next to the Chhota Shigri
273 glacier front (Azam et al., 2016). Measured with an automatic precipitation gauge (i.e. capturing all
274 precipitation forms), the authors found that the majority of precipitation was during the winter season,
275 and that the summer monsoon contributed with only 12 % to the annual precipitation. Based on these
276 observation estimates, and the similarities with our Sunderdhunga AWS precipitation patterns, we
277 estimate that about 800 ± 200 mm is a characteristic annual precipitation amount close to where the pits
278 were dug. If the precipitation amounts derived to explain the deposited EC in each pit is divided by 800
279 mm, the minimum number of years required to explain the EC observed in the pit is acquired. With this
280 approach it is clear that it would require decades of precipitation to explain the EC in the enriched LAP
281 layers in pits A and C. This is unrealistic, especially when the lower levels in pit F from the previous
282 year is compared. Even the difference in EC amount between pits B, E, and D compared to F is much
283 greater than can be explained from aggregating the EC accumulated by one year of precipitation in a
284 single melt layer. At the same time, the dry deposition of EC probably accounts for ~~only a few percent~~
285 ~~of the deposition~~ **about 7% of the total deposition**. With a dry deposition velocity of EC of 0.3 mm/s
286 (Emerson et al., 2018) and an atmospheric concentration of $0.3 \mu\text{g m}^{-3}$, reported at similar altitude at
287 the Nepal Pyramid station during the pre-monsoon (Bonasoni et al., 2010), the dry deposition can be
288 estimated to $2800 \mu\text{g m}^{-2}$ annually, which in **comparison to the BC wet deposition, is on the order of 40**

289 000 $\mu\text{g m}^{-2}$ annually (obtained by multiplying our 50 $\mu\text{g m}^{-2}$ per mm⁻¹ with our annual precipitation
290 estimate of 800 mm). Evidently the dry deposition is ~~which~~ several orders of magnitude lower than
291 what is encountered in the enriched LAP layers. Thus, this leads us to propose that EC must have been
292 transported laterally in the surface layer during the melt period in the summer of 2016 and converged
293 in the altitude range where the pits were dug. From Figure 1 it can be seen that the pits were dug in a
294 complex terrain where slopes with increasing gradient are reaching up to the summit towards the
295 southwest.

296

297 The data and analysis presented above lead us to propose that the old snow layers observed in pit F
298 from 2015 are the same old snow layers observed for the pits dug in 2016. The EC equivalent
299 precipitation profile of pit F presented in Figure 4 suggests that strong melting had taken place already
300 in summer 2015. Hence, the old snow is composed of snow from at least the season 2013-2014 (or
301 perhaps also earlier seasons). Stratigraphy analysis for pit F presented in Svensson et al. (2018)
302 suggested that the snow deposition represented five seasons. The amount of precipitation represented
303 by the EC deposition (cf. Figure 4) in the old snow is about 2200 mm, which suggests that the EC was
304 deposited over several seasons, but less than 5 seasons. Another strong melt took place in 2016, possibly
305 leading to melting all of the snow from the season 2015-2016. In addition, during the melting phase,
306 water and snow particulates could be transported down the slopes from areas of the glacier with steep
307 slopes. Because the steepness of the slope decreases towards the valley, this resulted in a convergence
308 of percolated material from areas above the sampling sites. The young snow is likely part of the 2016-
309 2017 winter season that had started to accumulate before the sampling in October 2016 was
310 commenced. This is confirmed by AWS data that indicates intermittent snow events in October 2016.
311 At the AWS location a seasonal snow cover was in place in December 2016.

312

313 3.3 Mineral dust fraction in snow

314 An initial inspection of the mineral fractional absorption on the filters did not reveal any special
315 common pattern in concentration between the different pits, except for the enriched LAP layer samples,
316 which appeared to have higher concentrations than the other samples. In Figure 5, the data is grouped
317 according to the pit stratigraphy classification, and although the absolute range of MD fractions in
318 young snow samples is very large (5 to 71 %), the quartile range is only between 32 to 48 % with a
319 median value of 39 %. The median value for old snow is somewhat larger at 46 %, along with the range
320 and quartiles, which are closer together, from 26 to 70 % and from 43 to 50 %, respectively. The range
321 of values for the enriched LAP layer are consistently higher compared to the other two snow types. The
322 median is 78 % with a range and quartiles of 48 to 95 % and 74 to 82 %, respectively. Note that from a
323 total of 95 samples only 16 are from the LAP layer. As with EC, MD has the propensity to remain at
324 the snow surface with melting (e.g. Doherty et al., 2013).

325
326
327
328
329
330
331
332
333
334
335
336
337
338
339
340
341
342
343
344
345
346
347
348
349
350
351
352
353
354
355
356
357
358
359
360

Due to the typically heavy loading of material on the filters obtained in the enriched LAP layer, those values should be taken with caution, however. Non-linear effects could skew the resulting light absorption fractions towards larger values since with a very heavy loading (dark filter) the contribution by remaining particles may be over-estimated. This is because the relative contribution by additional light absorbing material decreases as the amount of material increases on very dark filters. In an extreme case, black on black will not add any contribution. The larger range of values in young snow compared to old snow is possibly an effect from the geometric thickness of the sampled slabs, which are in young snow generally thinner than in old snow, and that the density of young snow is typically less than the density of old snow. This results in each of the sampled segments in young snow representing less deposition of both water and LAP and, therefore, presenting a larger variability. Nevertheless, the ensemble of data presents similar median values for both young and old snow. The median of the percentage of the mineral dust absorption f_D value for young and old snow samples together becomes 44 %. The specific absorption by minerals is expected to be orders of magnitude smaller than BC (e.g. Utry et al., 2015), and the same is expected with respect to EC. This suggests that the deposition of minerals in the snow is orders of magnitude larger than EC. If we simply scale our characteristic EC constants (EC_y^* and EC_o^*), with the median of f_D and the ratio between their specific mass absorption coefficients (MAC), according to:

$$\frac{f_D}{(1-f_D)} \frac{MAC_{EC}}{MAC_D} EC_c = D_c \quad (4)$$

we arrive at a mass concentration for minerals. We use a MAC for BC of $7.5 \text{ m}^2 \text{ g}^{-1}$ (Bond and Bergstrom, 2006). The MAC for the minerals is not known and can vary significantly, but for the sake of this test we use a MAC value representative for the mineral quartz with $0.0023 \text{ m}^2 \text{ g}^{-1}$ (Utry et al., 2015). If we use these values we arrive at a range of $128\text{-}384 \text{ } \mu\text{g g}^{-1}$ of minerals in the snow. This is in range with previous gravimetric observations from Himalaya (e.g. Thind et al., 2019; Zhang et al., 2018).

3.4 Discussion

Our results indicate that the contribution to light absorption by minerals can be comparable to light absorption by EC in the Sunderdhunga area at about 5 km altitude. This translates into a mass concentration ratio between EC and minerals of more than three orders of magnitude. These large ratios are typically not reported for air samples because much of the deposited minerals are likely from local sources. This supports a hypothesis of a positive climate feedback that results in a reduction of snow cover and the exposure to larger sources of minerals.

361 For the Tibetan plateau, Zhang et al. (2018) estimated that the retreat of the snow cover could be
362 advanced by more than a week due to LAP in snow. In their estimates, BC accounted for most of this
363 effect and dust advanced the melting by about one day. The BC concentration in snow used in their
364 calculations were about one order of magnitude larger than our derived values from the profiles in the
365 snow pits. This difference can be attributed to the significant contribution of aerosol particle dry
366 deposition in arid regions (Wang et al., 2014), but the range of values presented in their Table 2 reveals
367 a potential problem from sampling surface snow. Post depositional processes (e.g.
368 sublimation/evaporation, hoar formation, snow drift) can alter the concentration at a given location
369 relatively fast, which is less of a problem if a deeper layer of the snow pack is investigated instead of
370 solely the surface snow. Simply taking a larger vertical slab is not sufficient as is evident from the melt
371 layer in the present study. The enriched LAP layer in the pits can be studied to characterize the short-
372 term seasonal surface albedo, but the aerosol concentrations cannot be directly related to the deposition.
373 The consistency between pits and different sampling seasons in the integrated deposition profiles above
374 and below the enriched LAP layer show the strength in the data collected from snow pits in comparison
375 to snap-shot conditions of surface snow.

376

377 4 Conclusions

378 In this study we aimed at characterizing the observed deposition of EC in the glacier snow in the
379 Sunderdhunga valley and to estimate the contribution from minerals to LAP in the snow. The analysis
380 illustrates that in the sampling area of Durga Kot and Bhanolti glaciers, the deposition of EC in young
381 snow (from current winter season) is characterized by approximately $50 \mu\text{g m}^{-2} \text{mm}^{-1}$ SWE water, which
382 is in the range of other observations. The median fraction of light absorption caused by minerals was
383 about 39 % (Q1=32, Q3=48). In old snow (from previous winter seasons), the deposition was
384 characterized by about $150 \mu\text{g m}^{-2} \text{mm}^{-1}$ SWE water. The reason for this difference can simply be due
385 to a larger deposition in the years before sampling was conducted, or that more water had the chance to
386 leave the snow-pack of older snow. Different from young snow, old snow have had to survive at least
387 one summer season. The median fraction of light absorption was 46 % (Q1=43, Q3=50) by minerals in
388 the old snow layer. Although the variability within each layer is rather large, the obtained lower median
389 fraction for young snow is consistent with the fact that old snow is more exposed to rock surfaces free
390 of snow during the summer season.

391

392 Between these two layers of old and young snow, a clearly visible and very dark layer was present. This
393 layer was most likely a result of strong melting that took place in the summers of 2015 and 2016 as
394 discussed in 3.2. However, the high concentration of EC found in this layer cannot simply be explained
395 by a collapse of the snow-pack vertically, and thus it is concluded that lateral transport of LAP
396 (including EC and minerals) took place that resulted in a convergence of material in the altitude range

397 of the snow pits. Different from the other two layers (young and old snow), this enriched LAP layer
398 presented large differences with respect to EC content among the different pits. The fraction of light
399 absorption by minerals was the highest of the three layers and was about 80 % (Q1=74, Q3=82).

400

401 The profiles of EC and the mineral absorption fraction show good agreement between subsequent years
402 and among different pits. At the same time, the topography in this mountainous region of Himalaya
403 evidently causes great complexity with respect to the distribution of LAP in the snow surface layer
404 during periods of strong melt. Although data is limited in spatial and temporal dimensions our results
405 are useful for large scale radiation impact assessments of EC deposition and minerals. In small scale
406 regional studies, however, the effects of complex topography and spatial variability should be
407 considered separately. Future work should further study the mineral dust and its composition in the
408 area, in order to more accurately elucidate dust role in the snow radiation state in this part of the
409 Himalaya.

410

411 Data availability

412 All data are available upon request.

413

414 Author contributions

415 J. Sv, H.H, E.A., N.D., H.L., participated in the field expedition. S.T., R.H., V.S., M. L., H.L., A.H.
416 handled project administration. Data analysis was performed by J. Sv. and J. St. Funding acquisition:
417 A.H. Supervision M.L. and H.L. J. Sv led the writing of the manuscript with J. St., with input from all
418 other co-authors.

419

420 Competing interests.

421 The authors declare that they have no conflict of interest.

422

423 Acknowledgements

424 This work has been supported by the Academy of Finland project: Absorbing Aerosols and Fate of
425 Indian Glaciers (AAFIG; project number 268004), and the Academy of Finland consortium: “Novel
426 Assessment of Black Carbon in the Eurasian Arctic: From Historical Concentrations and Sources to
427 Future Climate Impacts” (NABCEA project number 296302). J.Svensson acknowledges support from
428 the two Finnish foundations: Maj and Tor Nessling and Oskar Huttunen; as well as the invited scientist
429 grant from the UGA. J. Ström is part of the Bolin Centre for Climate Research, and acknowledges the
430 Swedish Research Council grant 2017-03758. We are thankful for Daniela Tuomala’s work with the
431 filter analyzes, as well as the strenuous assistance given by Sherpas and mountain guides during the
432 expeditions to the Sunderdhunga valley.

433 References

- 434 Anders, A. M., Roe, G. H., Hallet, B., Montgomery, D. R., Finnegan, N. J., and Putkonen, J.: Spatial
435 patterns of precipitation and topography in the Himalaya, *Geol. Soc. Am. Special Papers*, 398, 39–53,
436 2006.
- 437 Azam, M. F., Ramanathan, A. L., Wagon, P., Vincent, C., Linda, A., Berthier, E., Sharma, P., Mandal,
438 A., Angchuk, T., Singh, V. B., and Pottakkal, J. G.: Meteorological conditions, seasonal and annual
439 mass balances of Chhota Shigri Glacier, western Himalaya, India, *Ann. Glaciol.*, 57, 328–338, doi:
440 10.3189/2016AoG71A570, 2016.
- 441 Bond, T. C., and Bergstrom, R. W.: Light absorption by carbonaceous particles: An investigative
442 review, *Aerosol Sci. Tech.*, 40, 27–67, doi:10.1080/02786820500421521, 2006.
- 443 Bonasoni, P., Laj, P., Marinoni, A., Sprenger, M., Angelini, F., Arduini, J., Bonafè, U., Calzolari, F.,
444 Colombo, T., Decesari, S., Di Biagio, C., di Sarra, A. G., Evangelisti, F., Duchi, R., Facchini, MC.,
445 Fuzzi, S., Gobbi, G. P., Maione, M., Panday, A., Roccatò, F., Sellegri, K., Venzac, H., Verza, G. P.,
446 Villani, P., Vuillermoz, E., and Cristofanelli, P.: Atmospheric Brown Clouds in the Himalayas: first
447 two years of continuous observations at the Nepal Climate Observatory-Pyramid (5079 m), *Atmos.*
448 *Chem. Phys.*, 10, 7515–7531, doi:10.5194/acp-10-7515-2010, 2010.
- 449 Bookhagen, B. and Burbank, D. W.: Toward a complete Himalayan hydrological budget:
450 Spatiotemporal distribution of snowmelt and rainfall and their impact on river discharge, *J. Geophys.*
451 *Res.*, 115, F03019, doi:10.1029/2009JF001426, 2010.
- 452 Carrico, C. M., Bergin, M. H., Shrestha, A., Dibb, J. E., Gomes, L., and Harris, J.M.: The importance
453 of carbon and mineral dust to seasonal aerosol properties in the Nepal Himalayas, *Atmos. Environ.*, 37,
454 2811–2824, 2003.
- 455 Chow, J. C., Watson, J. G., Crow, S., Lowenthal, D. H., and Merrifield, T.: Comparison of IMPROVE
456 and NIOSH carbon measurements, *Aerosol Sci. Tech.*, 34, 23–34, 2001.
- 457 Doherty, S. J., Grenfell, T. C., Forsström, S., Hegg, D. L., Brandt, R. E., and Warren, S. G.: Observed
458 vertical redistribution of black carbon and other insoluble light-absorbing particles in melting snow, *J.*
459 *Geophys. Res.-Atmos.*, 118, 5553–5569, doi.org/10.1002/jgrd.50235, 2013.
- 460 Emerson, E. W., Katich, J. M., Schwarz, J. P., McMeeking, G. R., and Farmer, D. K.: Direct
461 Measurements of Dry and Wet Deposition of Black Carbon Over a Grassland, *J. Geophys. Res.-Atmos.*,
462 123, 12277–12290, doi.org/10.1029/2018JD028954, 2018.
- 463 Flanner, M. G., Zender, C. S., Randerson, J. T., and Rasch, P. J.: Present-day climate forcing and
464 response from black carbon in snow, *J. Geophys. Res.-Atmos.*, 112, D11202,
465 doi.org/10.1029/2006JD008003, 2007.
- 466 Gertler, C. G., Puppala, S. P., Panday, A., Stumm, D., and Shea, J.: Black carbon and the Himalayan
467 cryosphere: A review, *Atmos. Environ.*, 125, 404–417, doi.org/10.1016/j.atmosenv.2015.08.078, 2016.
- 468 He, C., Flanner, M. G., Chen, F., Barlage, M., Liou, K.-N., Kang, S., Ming, J., and Qian, Y.: Black
469 carbon-induced snow albedo reduction over the Tibetan Plateau: uncertainties from snow grain shape
470 and aerosol–snow mixing state based on an updated SNICAR model, *Atmos. Chem. Phys.*, 18, 11507–
471 11527, doi.org/10.5194/acp-18-11507-2018, 2018.
- 472 Helfricht, K., Hartl, L., Koch, R., Marty, C., and Olfes, M.: Obtaining sub-daily new snow density from
473 automated measurements in high mountain regions, *Hydrol. Earth Syst. Sci.*, 22, 2655–2668,
474 doi.org/10.5194/hess-22-2655-2018, 2018.

475 Hooda, R.K., Kivekäs, N., O'Connor, E.J., Collaud Coen, M., Pietikäinen, J.P., Vakkari, V., Backman,
476 J., Henriksson, S.V., Asmi, E., Komppula, M., Korhonen, H., Hyvärinen, A. P., Lihavainen, H.: Driving
477 factors of aerosol properties over the foothills of central Himalayas based on 8.5 Years continuous
478 measurements, *J. Geophys. Res. Atmos.*, 123, doi.org/10.1029/2018JD029744, 421-13,442, 2018.

479 Jacobi, H.-W., Lim, S., Ménégoz, M., Ginot, P., Laj, P., Bonasoni, P., Stocchi, P., Marinoni, A., and
480 Arnaud, Y.: Black carbon in snow in the upper Himalayan Khumbu Valley, Nepal: observations and
481 modeling of the impact on snow albedo, melting, and radiative forcing, *The Cryosphere*, 9, 1685–1699,
482 doi.org/10.5194/tc-9-1685-2015, 2015.

483 Jacobson, M. Z.: Climate response of fossil fuel and biofuel soot, accounting for soot's feedback
484 to snow and sea ice albedo and emissivity, *J. Geophys. Res.-Atmos.*, 109, D21201,
485 doi.org/10.1029/2004jd004945, 2004.

486 Kaspari, S., Painter, T. H., Gysel, M., Skiles, S. M., and Schwikowski, M.: Seasonal and elevational
487 variations of black carbon and dust in snow and ice in the Solu-Khumbu, Nepal and estimated radiative
488 forcings, *Atmos. Chem. Phys.*, 14, 8089–8103, doi.org/10.5194/acp-14-8089-2014, 2014.

489 Krecl, P., Ström, J., and Johansson, C.: Carbon content of atmospheric aerosols in a residential area
490 during the wood combustion season in Sweden, *Atmos. Environ.*, 41, 6974–6985,
491 doi.org/10.1016/j.atmosenv.2007.06.025, 2007.

492 Kopacz, M., Mauzerall, D. L., Wang, J., Leibensperger, E. M., Henze, D. K., and Singh, K.: Origin and
493 radiative forcing of black carbon transported to the Himalayas and Tibetan Plateau, *Atmos. Chem.
494 Phys.*, 11, 2837–2852, doi.org/10.5194/acp-11-2837-2011, 2011.

495 Li, C., Bosch, C., Kang, S., Andersson, A., Chen, P., Zhang, Q., Cong, Z., Chen, B., Qin, D., and
496 Gustafsson, O.: Sources of black carbon to the Himalayan-Tibetan Plateau glaciers, *Nature Commun.*,
497 7, 12574, doi.org/10.1038/ncomms12574, 2016.

498 Ménégoz, M., Krinner, G., Balkanski, Y., Boucher, O., Cozic, A., Lim, S., Ginot, P., Laj, P., Gallée,
499 H., Wagnon, P., Marinoni, A., and Jacobi, H. W.: Snow cover sensitivity to black carbon deposition in
500 the Himalayas: from atmospheric and ice core measurements to regional climate simulations, *Atmos.
501 Chem. Phys.*, 14, 4237–4249, doi.org/10.5194/acp-14-4237-2014, 2014.

502 Mimeau, L., Esteves, M., Zin, I., Jacobi, H.-W., Brun, F., Wagnon, P., Koirala, D., and Arnaud, Y.:
503 Quantification of different flow components in a high-altitude glacierized catchment (Dudh Koshi,
504 Himalaya): some cryospheric-related issues, *Hydrol. Earth Syst. Sci.*, 23, 3969–3996,
505 doi.org/10.5194/hess-23-3969-2019, 2019.

506 Ming, J., Du, Z., Xiao, C., Xu, X., and Zhang, D.: Darkening of the mid-Himalaya glaciers since 2000
507 and the potential causes, *Environ. Res. Lett.*, 7, 014021, doi:10.1088/1748-25 9326/7/1/014021, 2012.

508 Ming, J., Xiao, C., Du, Z., and Yang, X.: An Overview of Black Carbon Deposition in High Asia
509 Glaciers and its Impacts on Radiation Balance, *Adv. Water Resour.*, 55, 80–87, 2013.

510 Petzold, A., Ogren, J. A., Fiebig, M., Laj, P., Li, S.-M., Baltensperger, U., Holzer-Popp, T., Kinne, S.,
511 Pappalardo, G., Sugimoto, N., Wehrli, C., Wiedensohler, A., and Zhang, X.-Y.: Recommendations for
512 reporting "black carbon" measurements, *Atmos. Chem. Phys.*, 13, 8365–8379, doi.org/10.5194/acp-13-
513 8365-2013, 2013.

514 Raatikainen, T., Hyvärinen, A. P., Hatakka, J., Panwar, T. S., Hooda, R. K., Sharma, V. P., and
515 Lihavainen, H.: The effect of boundary layer dynamics on aerosol properties at the Indo-Gangetic plains
516 and at the foothills of the Himalayas, *Atmos. Environ.*, 89, 548– 555,
517 doi.org/10.1016/j.atmosenv.2014.02.058, 2014.

518 Ramanathan, V. and Carmichael, G.: Global and regional climate changes due to black carbon, *Nat.*
519 *Geosci.*, 1, 221–227, doi.org/10.1038/ngeo156, 2008.

520 Santra, S., Verma, S., Fujita, K., Chakraborty, I., Boucher, O., Takemura, T., Burkhart, J. F., Matt, F.,
521 and Sharma, M.: Simulations of black carbon (BC) aerosol impact over Hindu Kush Himalayan sites:
522 validation, sources, and implications on glacier runoff, *Atmos. Chem. Phys.*, 19, 2441–2460,
523 doi.org/10.5194/acp-19-2441-2019, 2019.

524 Sarangi, C., Qian, Y., Rittger, K., Bormann, K. J., Liu, Y., Wang, H., Wan, H., Lin, G., and Painter, T.
525 H.: Impact of light-absorbing particles on snow albedo darkening and associated radiative forcing over
526 high-mountain Asia: high-resolution WRF-Chem modeling and new satellite observations, *Atmos.*
527 *Chem. Phys.*, 19, 7105–7128, doi.org/10.5194/acp-19-7105-2019, 2019.

528 Skiles, S. M., Flanner, M., Cook, J. M., Dumont, M., and Painter, T. H.: Radiative forcing by light-
529 absorbing particles in snow, *Nat. Clim. Change*, 8, 964–971, doi.org/10.1038/s41558-018-0296-5,
530 2018.

531 Stigter, E. E., Maxime Litt, A., Jakob Steiner, F., Pleun Bonekamp, N. J., Joseph Shea, M., and
532 Immerzeel, W. W.: The importance of snow sublimation on a himalayan glacier. *Front. Earth Sci.* 6:108,
533 doi: 10.3389/feart.2018.00108, 2018.

534 Svensson, J., Ström, J., Kivekäs, N., Dkhar, N. B., Tayal, S., Sharma, V. P., Jutila, A., Backman, J.,
535 Virkkula, A., Ruppel, M., Hyvärinen, A., Kontu, A., Hannula, H.-R., Leppäranta, M., Hooda, R. K.,
536 Korhola, A., Asmi, E., and Lihavainen, H.: Light-absorption of dust and elemental carbon in snow in
537 the Indian Himalayas and the Finnish Arctic, *Atmos. Meas. Tech.*, 11, 1403–1416,
538 doi.org/10.5194/amt-11-1403-2018, 2018.

539 Thind, P. S., Chandel, K. K., Sharma, S. K., Mandal, T. K., and John, S.: Light-absorbing impurities in
540 snow of the Indian Western Himalayas: impact on snow albedo, radiative forcing, and enhanced
541 melting, *Environ. Sci. Pollut. Res. Int.*, 26, 7566–7578, doi.org/10.1007/s11356-019-04183-5, 2019.

542 Utry, N., Ajtai, T., Pintér, M., Tombácz, E., Illés, E., Bozóki, Z., and Szabó, G.: Mass-specific optical
543 absorption coefficients and imaginary part of the complex refractive indices of mineral dust components
544 measured by a multi-wavelength photoacoustic spectrometer, *Atmos. Meas. Tech.*, 8, 401–410,
545 doi.org/10.5194/amt-8-401-2015, 2015.

546 Wang, Z. W., Gallet, J. C., Pedersen, C. A., Zhang, X. S., Ström, J., and Ci, Z. J.: Elemental carbon in
547 snow at Changbai Mountain, northeastern China: concentrations, scavenging ratios, and dry deposition
548 velocities, *Atmos. Chem. Phys.*, 14, 629–640, doi.org/10.5194/acp-14-629-2014, 2014.

549 Warren, S. and Wiscombe, W.: A model for the spectral albedo of snow II. Snow containing
550 atmospheric aerosols, *J. Atmos. Sci.*, 37, 2734–2745, 1980.

551 Xu, B., Cao, J., Hansen, J., Yao, T., Joswiak, D.R., Wang, N., Wu, G., Wang, M., Zhao, H., Yang, W.,
552 Liu, X., and He, J.: Black soot and the survival of Tibetan glaciers, *P. Natl. Acad. Sci. USA*, 106,
553 22114–22118, doi.org/10.1073/pnas.0910444106, 2009.

554 Zhang, R., Wang, H., Qian, Y., Rasch, P. J., Easter, R. C., Ma, P.-L., Singh, B., Huang, J., and Fu, Q.:
555 Quantifying sources, transport, deposition, and radiative forcing of black carbon over the Himalayas
556 and Tibetan Plateau, *Atmos. Chem. Phys.*, 15, 6205–6223, doi.org/10.5194/acp-15-6205-2015, 2015.

557 Zhang, Y., Kang, S., Sprenger, M., Cong, Z., Gao, T., Li, C., Tao, S., Li, X., Zhong, X., Xu, M., Meng,
558 W., Neupane, B., Qin, X., and Sillanpää, M.: Black carbon and mineral dust in snow cover on the
559 Tibetan Plateau, *The Cryosphere*, 12, 413–431, doi.org/10.5194/tc-12-413-2018, 2018.

560 Table 1. Snow pit details from Sunderdhunga valley. Durga Kot glacier snow pits are A-B, while C-F are from Bhanolti glacier.

561

Snow pit ID and elevation (m a.s.l)	Depth interval (cm)	Snow density (g cm ⁻³)		Water equivalent (mm m ⁻²)	TC analyzed (μg L ⁻¹)	EC (μg L ⁻¹)		EC deposition (μg m ⁻²)	fD (%)
		Measured	Assumed			Analyzed	Reconstructed		
A, 5055	0-3	0.38		11.4	1130	55	-	632	24.6
	3-6	0.38		11.4	238	18	-	207	29.2
	6-9	0.35		10.5	477	47	-	495	40.4
	9-12	0.37		11.1	30300	-	3027	33596	-
	12-15	0.39		11.7	1307404	-	130740	1529663	76.1
	15-20		0.50	25.0	68177	-	6818	170442	55.1
	20-25		0.50	25.0	1398	278	-	6945	47.9
	25-30		0.50	25.0	1549	147	-	3684	49.8
	30-35		0.50	25.0	1769	271	-	6787	41.9
	35-40		0.50	25.0	1466	251	-	6273	46.5
	40-45		0.50	25.0	883	141	-	3528	44.6
	45-50		0.50	25.0	751	142	-	3553	43.1
	50-60		0.50	50.0	1090	171	-	8544	51.5
60-70		0.50	50.0	763	88	-	4412	45.9	
B, 5055	0-3	0.40		12.0	1542	95	-	1143	38.3
	3-6	0.40		12.0	693	30	-	364	27.5
	6-9	0.39		11.6	31710	-	712	8229	77.8
	9-12	0.33		9.9	69667	-	6967	68970	75.0
	12-15	0.33		9.9	3498	-	350	3463	50.6
	15-19		0.50	20.0	-	-	263	5269	49.9
	19-29		0.50	50.0	1534	246	-	12319	49.8
	29-39		0.50	50.0	1295	190	-	9480	46.2
	39-49		0.50	50.0	1517	248	-	12407	52.1

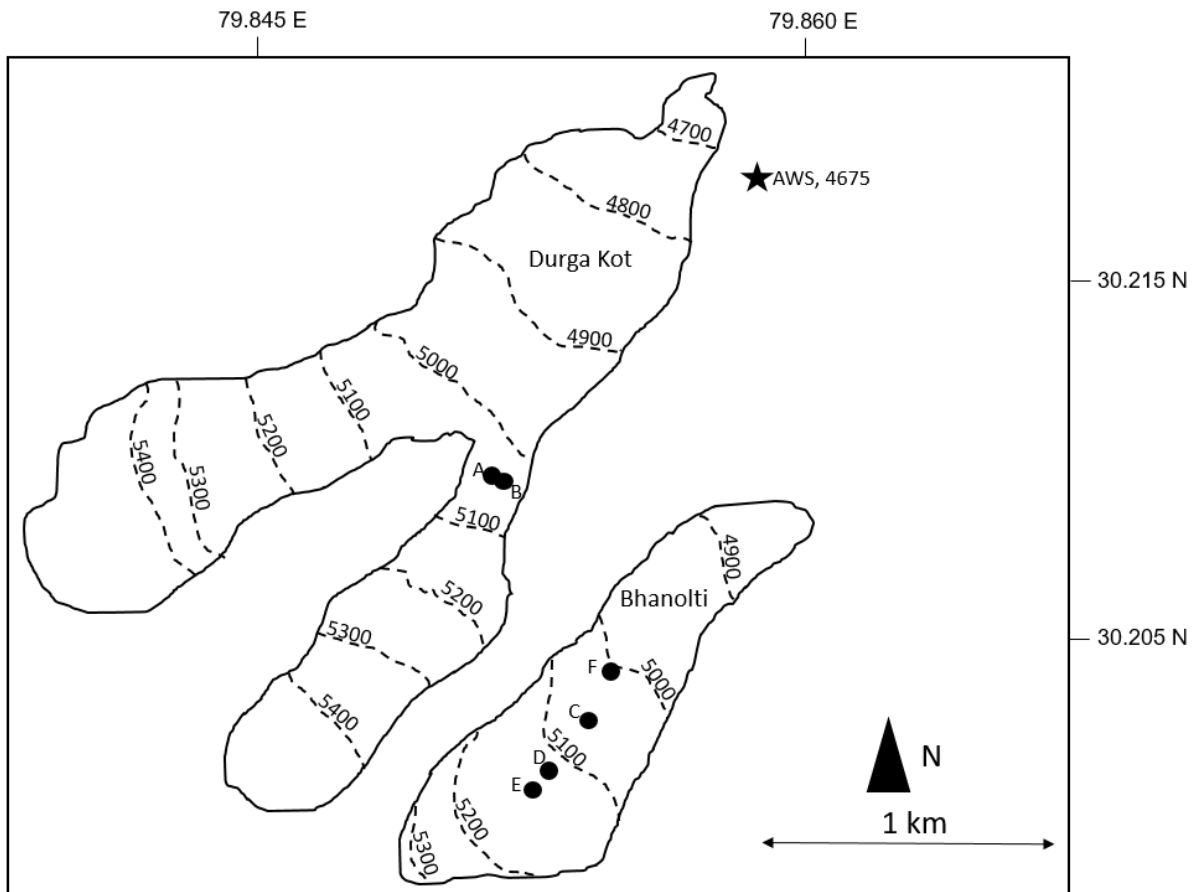
	49-59		0.50	50.0	1753	182	-	9100	40.2
	59-69		0.50	50.0	733	103	-	5156	41.2
	69-79		0.50	50.0	730	102	-	5121	44.9
C, 5068	0-3	0.40		12.0	2386	-	239	2864	47.6
	3-6	0.39		11.7	590	45	-	523	31.6
	6-11	0.39		19.5	372	34	-	658	59.4
	11-16	0.42		21.0	799	93	-	1959	54.8
	16-21	0.46		23.0	1074	141	-	3240	58.0
	21-26		0.50	25.0	1047065	-	107865	2617662	-
	26-31		0.50	25.0	4480	370	-	9257	62.0
	31-36		0.50	25.0	684	80	-	1988	58.9
	36-41		0.50	25.0	906	150	-	3746	43.6
	41-46		0.50	25.0	658	126	-	3159	44.2
	46-56		0.50	50.0	863	137	-	6871	43.5
	56-66		0.50	50.0	1191	156	-	7803	45.7
	66-76		0.50	50.0	832	144	-	7222	44.9
	76-86		0.50	50.0	802	94	-	4709	45.9
	86-96		0.50	50.0	416	51	-	2543	42.6
	96-106		0.50	50.0	609	78	-	3913	45.3
	106-116		0.50	50.0	692	76	-	3821	50.0
	116-126		0.50	50.0	500	46	-	2322	57.9
	126-136		0.50	50.0	1265	108	-	5386	59.0
D, 5125	0-3	0.39		11.7	1135	127	-	1487	35.2
	3-6	0.39		11.7	1012	91	-	1068	34.0
	6-9	0.37		11.1	449	30	-	337	42.6
	9-12	0.37		11.1	810	41	-	450	47.3
	12-15	0.37		11.0	1089	84	-	916	48.5
	15-18	0.37		11.0	357	32	-	353	38.6
	18-21	0.36		10.8	918	59	-	637	38.5
	21-24	0.42		12.6	274		27	346	70.8
	24-27	0.42		12.6	322	23	-	293	57.2

	27-30	0.36		10.8	443	28	-	297	36.3
	33-36	0.36		10.8	2393		239	2585	95.1
	36-39	0.45		13.5	1714		171	2314	77.6
	39-42	0.45		13.5	6806		681	9188	77.1
	42-44		0.50	10.0	177424		17742	177424	-
	44-49		0.50	20.0	9733		973	19465	60.1
	49-54		0.50	25.0	5708	665	-	16635	59.5
	54-59		0.50	25.0	1743	232	-	5798	69.6
	59-69		0.50	50.0	901	129	-	6459	46.1
E, 5143	0-3	0.33		9.9	992	128	-	1268	35.9
	3-6	0.33		9.9	422	63	-	622	41.4
	6-9	0.37		11.1	891	81	-	903	25.9
	9-12	0.31		9.3	569	41	-	380	43.0
	12-15	0.31		9.3	806	73	-	681	27.7
	15-18	0.29		8.7	750	35	-	302	41.0
	18-21	0.29		8.7	345	22	-	193	55.6
	21-24	0.39		11.7	644		64	754	4.5
	24-27	0.38		11.4	500	50	-	566	27.0
	27-30	0.38		11.4	439	65	-	739	56.7
	30-33	0.40		12.0	395	53	-	635	49.4
	33-36	0.40		12.0	642	26	-	308	27.3
	36-39	0.44		13.2	397	33	-	430	38.9
	39-42	0.44		13.2	1250	53	-	705	34.8
	42-45	0.44		13.2	1148	75	-	988	48.4
	45-48	0.45		13.5	828	169	-	2287	81.1
	48-51	0.45		13.5	901	131	-	1775	77.7
	51-54	0.45		13.5	617	58	-	786	85.8
	54-55	0.45		4.5	-	-	4540	20431	85.8
	55-60		0.50	25.0	69606	-	6961	174016	85.8
F, 5008	0-3		0.35	10.5	4075	-	408	4279	77.9
	3-6		0.40	12.0	4821	-	482	5785	60.8

6-10	0.40	16.0	17686		1769	28298	69.5
10-15	0.50	25.0	3555	-	356	8888	60.3
15-20	0.50	25.0	859	111		2786	33.1
20-30	0.50	50.0	1324	141		7036	49.2
30-40	0.50	50.0	807	106		5278	39.6
40-50	0.50	50.0	890	98		4907	36.7
50-60	0.50	50.0	2825	270		13484	49.5
60-70	0.50	50.0	1228	179		8965	39.9
70-80	0.50	50.0	696	93		4650	36.1
80-90	0.50	50.0	483	73		3640	35.8
90-100	0.50	50.0	1190	144		7190	43.9
100-110	0.50	50.0	652	79		3965	29.5
110-120	0.50	50.0	554	57		2846	25.7

562

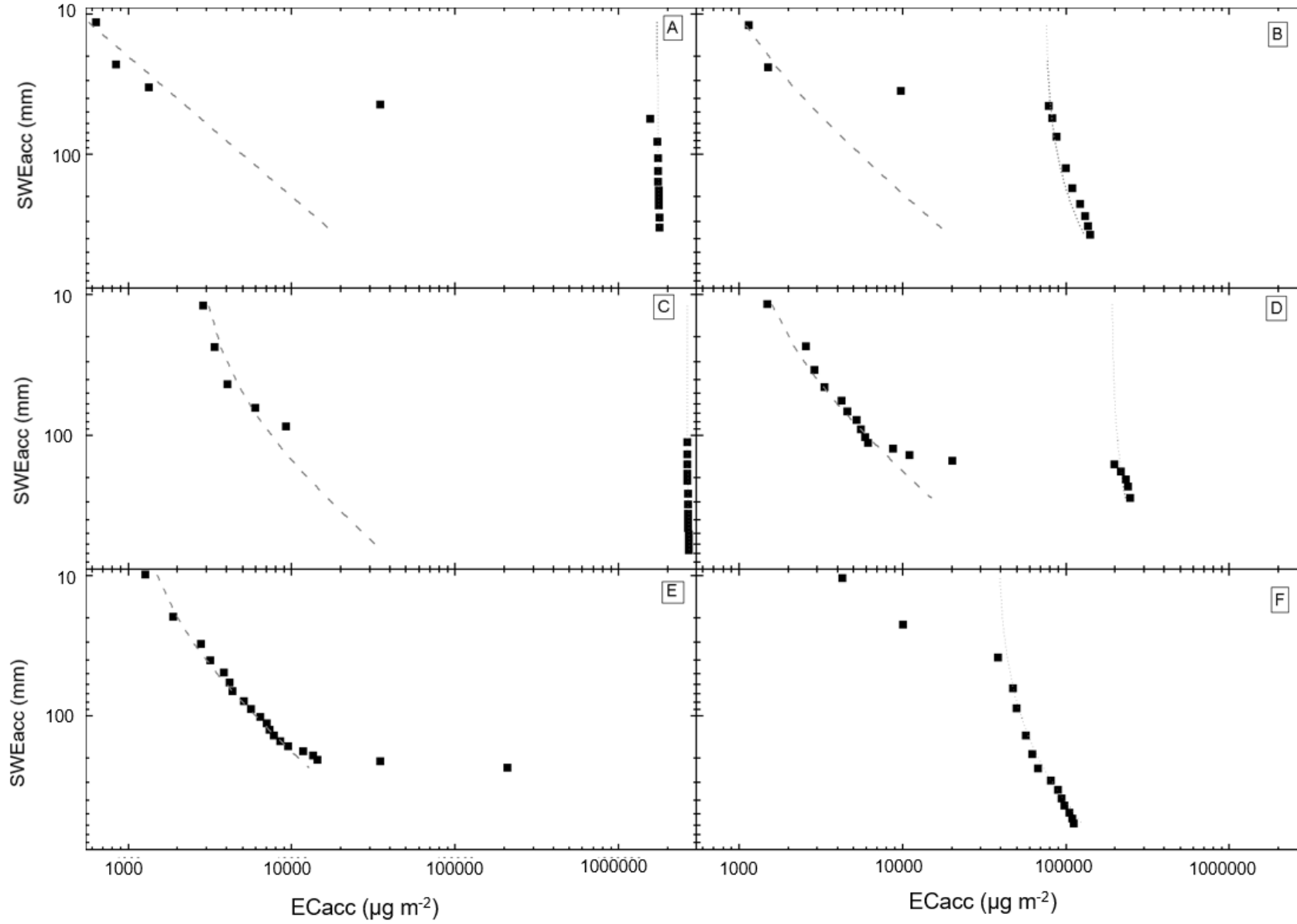
563



564

565

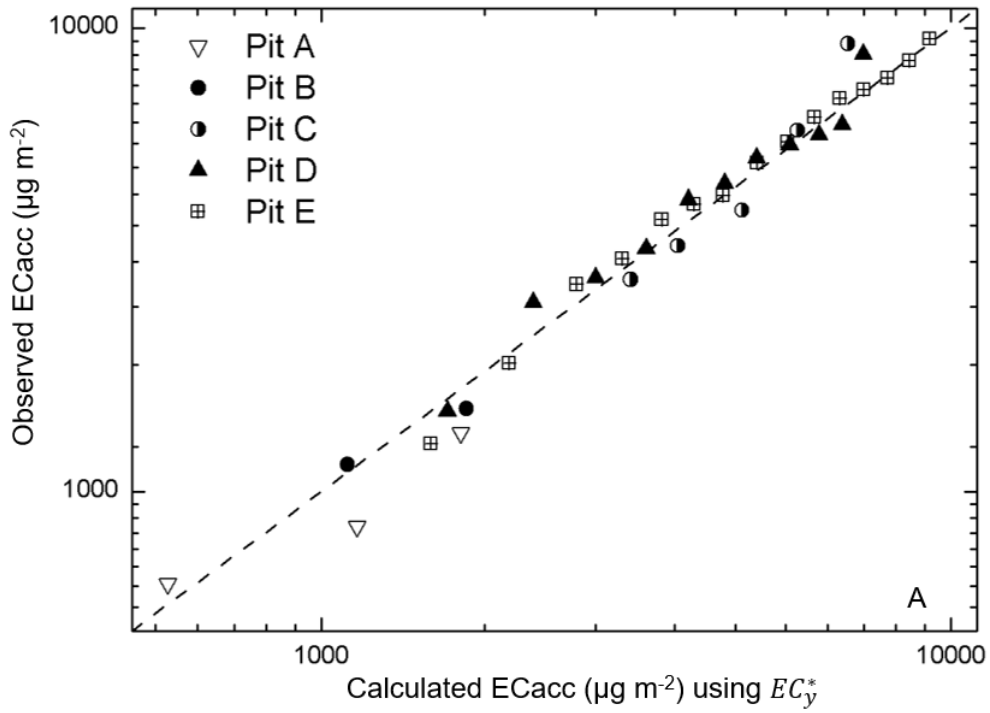
566 Figure 1. Map of glaciers with the location of the snow pits (black dots) and AWS indicated with a star.
 567 Dashed lines on the glacier refer to iso-lines .



569 Figure 2. The cumulative \widehat{EC}_i (ECacc) from top to bottom in the snow pits as function of accumulated d_{SWEi} expressed as SWEacc (mm): (a) Pit A, (b) Pit B, (c)
570 Pit C, (d) Pit D, (e) Pit E, (f) Pit F. The upper dashed line represents a constant deposition EC_y^* and the lower dashed-dotted line represents a constant deposition
571 EC_o^* . In pit E there were no snow samples classified as old snow, hence there is no EC_o^* line, while in in pit F there were no young snow samples, therefore no
572 EC_y^* line.

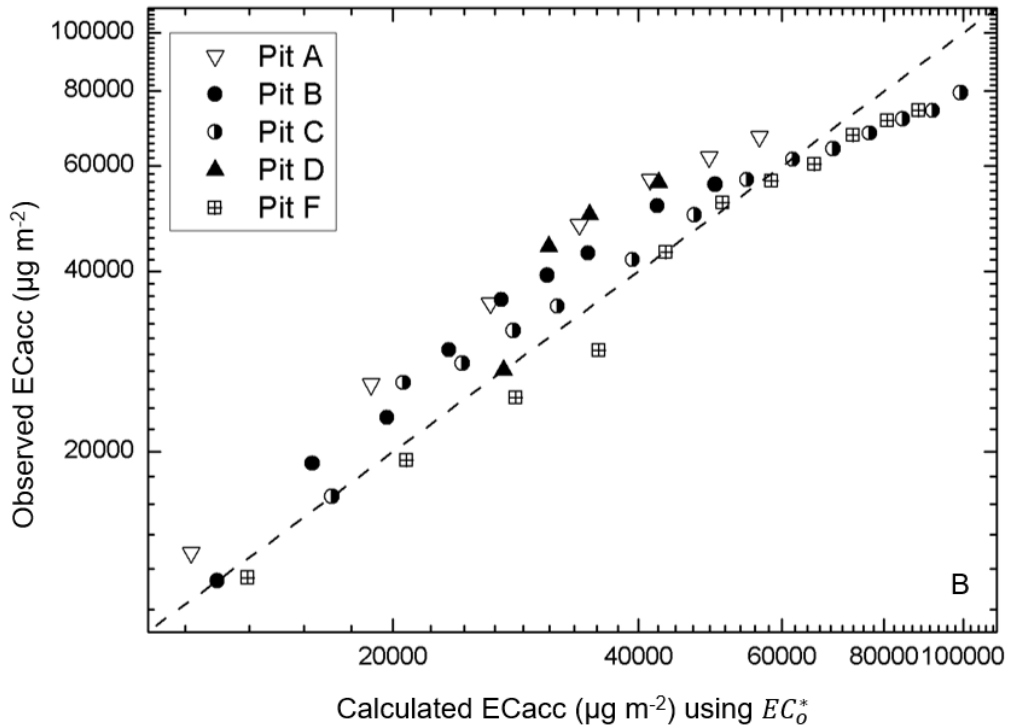
573

574



575

576

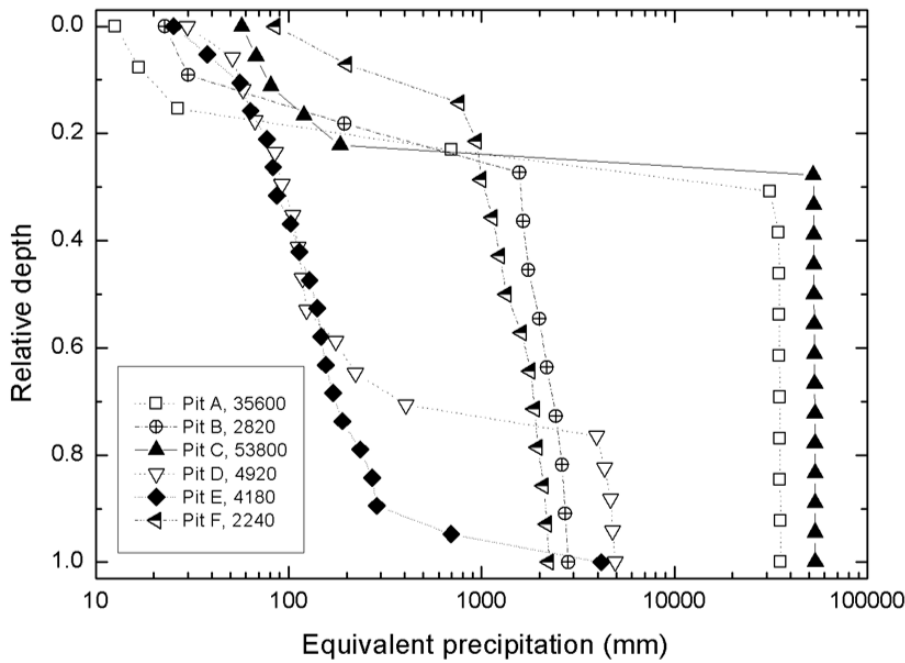


577

578 Figure 3. Observed and the calculated deposition using the constant deposition EC_y^* for young (a) and
579 EC_o^* for old (b) snow samples. Dashed lines indicate a 1:1 slope.

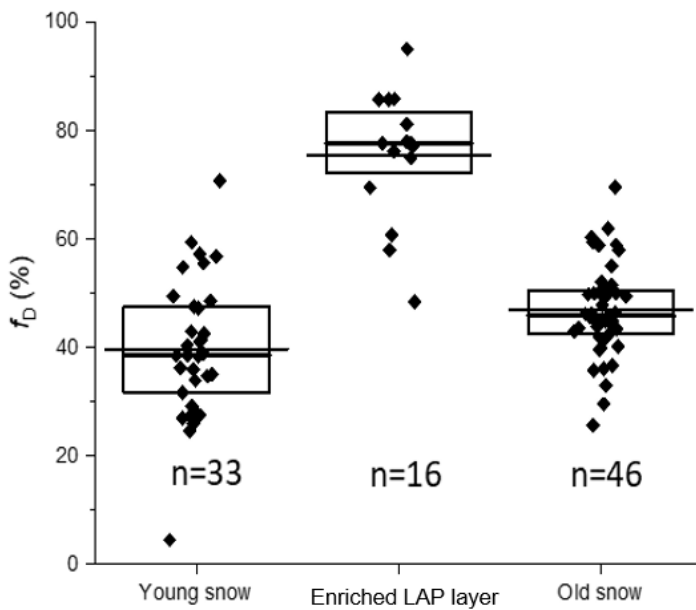
580

581
582
583



584
585
586
587
588

Figure 4. Equivalent precipitation for each pit based on a constant deposition EC_y^* in fresh snow as function of the relative depth of the pit from top to bottom.



589
590
591

Figure 5. Fractional dust absorption remaining after burning the filters during OC/EC analysis. The diamonds are individual values for each filter and the thin extended line represents the arithmetic

592 average. The box and thicker line represent the quartile range and median, respectively. The number
593 of samples are indicated in the figure as (n).